ORIGINAL PAPER

Fleurice Parat · François Holtz

Sulfur partitioning between apatite and melt and effect of sulfur on apatite solubility at oxidizing conditions

Abstract The effect of sulfur on phosphorus solubility in rhyolitic melt and the sulfur distribution between apatite, ± anhydrite, melt and fluid have been determined at 200 MPa and 800–1,100 °C via apatite crystallization and dissolution experiments. The presence of a small amount of sulfur in the system (0.5 wt.% S) under oxidizing conditions increases the solubility of phosphorus in the melt, probably due to changing calcium activity in the melt as a result of the formation of Ca-S complexing cations. Apatite solubility geothermometers tend to overestimate temperature in Ca-poor, S-bearing system at oxidizing conditions. In crystallization experiments, the sulfur content in apatite decreases with decreasing temperature and also with decreasing sulfur content of the melt. The sulfur partition coefficient between apatite and rhyolitic melt increases with decreasing temperature ($Kd_S^{apatite/melt} = 4.5$–$14.2$ at T = 1,100–900 °C) under sulfur-undersaturated conditions (no anhydrite). The sulfur partition coefficient is lower in anhydrite-saturated melt (~8 at 800 °C) than in anhydrite-undersaturated melt, suggesting that $Kd_S^{apatite/melt}$ depends not only on the temperature but also on the sulfur content of the melt. These first results indicate that the sulfur content in apatite can be used to track the evolution of sulfur content in a magmatic system at oxidizing conditions.

Introduction

Sulfur is an ubiquitous constituent of magmatic systems but is of particular interest because of its influence on

F. Parat (✉) · F. Holtz
Institut für Mineralogie, Universität Hannover, Callinstrasse 3, 30167 Hannover, Germany
E-mail: f.parat@mineralogie.uni-hannover.de

petrologic, volcanic, atmospheric, and ore-forming processes. Experimental data and observations on volatile-bearing systems indicate that sulfur fugacities in C-O-H-S- bearing magmatic systems can influence physical and chemical properties of magmas, volcanic eruption styles, and sulfur released into the atmosphere (e.g. Johnson et al. 1994; Scaillet et al. 1998). Although available data allow the evaluation of the behavior of H_2O and CO_2 in rocks under magmatic conditions (e.g. Blank and Brooker 1994; Papale 1999; Tamic et al. 2001), systematic data on sulfur (S) solubility in magmas and on sulfur behavior at subsolidus conditions are scarce, and more difficult to interpret because of the large number of interrelated intensive and extensive variables (e.g. pressure, temperature, melt composition, fugacities of oxygen, water, and sulfur) that can affect sulfur solubility behavior. Following the recent eruptions of anhydrite-bearing tephra at El Chichòn and Pinatubo volcanoes, accompanied by large injections of sulfur into the atmosphere, some experiments were done to determine phase equilibria of sulfur-rich magma and to estimate the sulfur content of the melt prior to the eruption (e.g. Carroll and Rutherford 1987; Luhr 1990; Scaillet and Evans 1999). Most of them attempted to characterize sulfur behavior in anhydrite- and pyrrhotite-bearing magmatic systems at relatively reducing conditions. However, most sulfur-rich magmatic systems are related to subduction-zones, are fluid-saturated, and highly oxidized.

One approach to the estimation of the sulfur budget in hydrous and highly oxidized volcanic systems and to the determination of the sulfur distribution during magmatic differentiation and eruption is to consider early-crystallized sulfur-bearing minerals. Primary volcanic anhydrite is readily lost from the geological record because it is rapidly dissolved by rainwater after eruption (Luhr et al. 1984) or by late hydrothermal magmatic fluids in the plutonic environment. In contrast, apatite, which can incorporate sulfur as sulfate, is a resistant mineral, occurs widely, and is early crystallized. Thus, apatite is a potential tool to record sulfur activity in

magmatic systems (e.g. Streck and Dilles 1998; Parat et al. 2002). The ability of magmatic apatite to concentrate geochemically important elements such as the rare earth elements has been well documented and has led to several experimental investigations of the chemical behavior of this common accessory phase during the generation and evolution of mafic, intermediate, and felsic magmas (Watson 1979; Harrison and Watson 1984; Pichavant et al. 1992). These experimental studies constrain the potential role of apatite in magma genesis and evolution by establishing its solubility in common magmas as a function of melt composition, temperature, and pressure. All quantitative experiments on apatite solubility have been performed via apatite dissolution only (product from crystallization experiments could not be analyzed, Pichavant et al. 1992) and demonstrate that apatite solubility decreases with decreasing temperature, and decreases with increasing Si contents, but increases with Alumina Saturation Index (ASI = Al/(Ca + Na + K) (mole proportion)).

In order to use sulfur concentration in apatite as a geochemical tracer, we carried out a series of experiments to estimate the effect of sulfur on apatite solubility and the distribution of sulfur between S-rich apatite, melt, and fluid. Both apatite dissolution and apatite crystallization experiments have been performed at temperatures from 800 to 1,100 °C at oxidizing conditions with S-free and S-bearing haplogranitic glass. The results have implications for the estimation of melt sulfur contents prior to eruption.

Starting materials and experimental method

Preparation of charges

The starting material composition used for all experiments is a synthetic SiO_2-Al_2O_3-Na_2O-K_2O melt close to that of typical iron-poor rhyolitic melts (e.g. Erevan Dry Fountain Obsidian, Armenia; Bagdassarov and Dingwell 1993; Stevenson et al. 1995). This initial composition is also close to those used by Harrison and Watson (1984) and Wolf and London (1994) for apatite solubility studies. The synthetic starting material (glass 6, Table 1) was prepared from powders of $NaCO_3$, K_2CO_3, Al_2O_3, and SiO_2 and by two cycles of melting at 1,600 °C and 1 atm ($\sim$25 h and 4 h with grinding between the two fusions). Its CIPW normative composition is $Qz_{35}Ab_{36}Or_{29}$, with measured ASI of $\sim$1.03 (Table 1).

Apatite crystallization experiments

Natural apatite from Tyrol (grain size < 50 μm), with a composition close to $Ca_5(PO_4)_3F$ (Table 1), was mixed with P- and Ca-free haplogranitic synthetic glass (glass 6, Table 1) and heated at 1,300 °C and 1 atm. for 3 days. The resulting glass (glass 7, Table 1) was checked with a back-scattered electron image to verify the complete dissolution of crystals and analyzed with a microprobe for homogeneity. Loss of alkalis was minimal after heating (e.g. < 0.13 wt.% Na_2O). The synthetic glass was carefully crushed and 30 mg was loaded into an Au-capsule for experiments performed at 800, 900, and 1,000 °C and in an AuPd-capsule for experiments performed at 1,100 °C (all capsules have a 2.8 cm inner diameter and 2 cm length), with 10 wt.% of pure H_2O and 0.5 wt.% of sulfur as elemental S for sulfur-bearing experiments.

Table 1 Starting material

	Glass 6 P_2O_5-free CaO-free	Glass 7 Glass 6 + 4 wt.% apa	Apatite
wt.%			
SiO_2	77.34	75.72	0.02
TiO_2	–	–	0.04
Al_2O_3	12.63	12.28	0.01
FeO	–	–	0.05
MnO	–	–	0.09
MgO	–	–	0.05
CaO	–	2.24	55.80
Na_2O	4.24	3.54	0.02
K_2O	4.85	4.74	0.01
P_2O_5	–	1.64	42.10
F	–	0.04	3.22
Cl	–	–	0.04
Total	99.08	100.20	101.45
O-F, Cl	–	–	1.05
Total	–	–	100.41
ASI	1.03	0.82	–
A/CNK	1.03	0.64	–
Ca/P	–	1.73	1.68

A/CNK = Al/(Na + K + 2Ca); ASI = (Al/(Na + Ca + K))

The amount of water was chosen so as to reach H_2O-saturated conditions in S-free melt (Holtz et al. 2001). Upon loading, capsules were sealed by arc welding, surrounded with wet paper and frozen into nitrogen to avoid water loss. The capsules were weighted to check for leakage after welding and after drying for 1 h at 110 °C. After completion of the experiments, capsules were weighted again to ensure closed-system behavior at high P and T.

Apatite dissolution experiments

Apatites from Tyrol were crushed and sieved to a grain size between 42 and 70 μm to ensure homogeneous population and to reduce problems of apatite contamination during electron microprobe analyses of experimental glasses. Four wt.% of apatite were mixed with P- and Ca-free haplogranitic glass (glass 6, Table 1). A mixture of synthetic glass and apatite was loaded into an Au- or AuPd-capsule with 10 wt.% of pure H_2O and 0.5 wt.% of sulfur as S for sulfur-bearing experiments and sealed by arc welding as described for apatite crystallization experiments.

Experimental procedure

Apatite crystallization and apatite dissolution experiments were performed simultaneously. The investigated temperatures were 800, 900, 1,000, and 1,100 °C and the experimental pressure condition was 200 MPa (Table 2). The redox state was chosen to be very oxidized to have sulfur as sulfate species as apatite incorporates S as sulfate (SO_4^{2-}). At T≥900 °C, an internally heated pressure vessel (IHPV) working vertically, pressurized with argon was used. The intrinsic oxygen fugacity is NNO + 3.7 (expressed as Δlog f_{O2}) as determined at 200 MPa and from 900 to 1,200 °C in the IHPV by Berndt et al. (2004) using the Ni-Pd solid sensors (Taylor et al. 1992). The IHPV was heated by a two-loop furnace made of molybdenum. Temperatures were continuously recorded by internal K-type thermocouples and are known within ± 10 °C. Pressure was measured with a strain-gauge manometer (accuracy ± 50 bar). Samples were quenched by turning off the power resulting in an average cooling rate of 150°C/min down to 400 °C. Constant pressure was maintained during cooling by automatic pumping. All experiment durations were 7 days to ensure equilibrium and only one experiment was performed at 1,000 °C during 1 day to characterize the exchange reaction during apatite dissolution (see discussion).

Table 2 Experimental conditions and results

Run	Duration (days)	T (°C)	S added in (wt.%)	Results**	S in apatite* (ppm)	S in melt* (ppm)	S in Fluid** (wt.%)	H$_2$0 in Fluid** (wt.%)	Kd$_s$ Fluid/melt	Kd$_s$ apatite/melt
Crystallization experiments – oxidizing conditions – 200 MPa										
#46	14	800	–	Apatite microlith (1–5um, ∽3.5 wt.%)						
#47	14	800	0.5	Apatite microcryst (10um, ∽2.5 wt.%) + anhydrite (∽1.5 wt.%)	2,881	353	8.88	91.12	252	8.2
#34	7	900	–	Apatite microlith (1–5um, ∽3.25 wt.%)						
#35	7	900	0.5	Apatite crystal (up to 40 um, ∽3.1 wt.%)	1,780	125	7.33	92.67	586	14.2
#26	7	1,000	–	Apatite microlith (1–5um, ∽3.2 wt.%)						
#27	7	1,000	0.5	Apatite crystal (up to 40 um, ∽2.9 wt.%)	2,559	344	7.06	92.94	205	7.4
#50	7	1,100	–	Apatite microlith (1–5um, ∽2.3 wt.%)						
#51	7	1,100	0.5	Apatite crystal (up to 40 um, ∽2.25 wt.%)	2,884	646	6.99	93.01	108	4.5
Dissolution experiments – oxidizing conditions – 200 MPa										
#48	14	800	–	Apatite (∽2.7 wt.%)						
#49	14	800	0.5	Apatite (∽3.7 wt.%) + anhydrite (∽1.6 wt.%)	–	363	8.81	91.19	243	–
#36	7	900	–	Apatite (∽3.6 wt.%)						
#37	7	900	0.5	Apatite (∽3.5 wt.%)	–	160	8.31	91.69	520	–
#28	7	1,000	–	Apatite (∽3.4 wt.%)						
#29	7	1,000	0.5	Apatite (∽3.3 wt.%)	–	487	6.96	93.04	143	–
#52	7	1,100	–	Apatite (∽3.1 wt.%)						
#53	7	1,100	0.5	Apatite (∽2.8 wt.%)	–	637	6.69	93.31	105	–
#54	1	1,000	–	Apatite (∽3.6 wt.%)						
#55	1	1,000	0.5	Apatite (∽3.5 wt.%)						

*: microprobe analyses, **: Mass balance calculations ($\Sigma r^2 < 0.2$; errors: ± 0.2))

Experiments at 800 °C were performed in horizontally oriented cold-seal pressure vessels (CSPV) made of Ni-rich alloy and pressurized with argon during 14 days. At 800–840 °C and 200 MPa, the $\Delta\log f_{O_2}$ measured with sensor capsules (Taylor et al. 1992) was found to be NNO + 2.3 (Berndt et al. 2001). Temperatures were continuously recorded by external K-type thermocouples and are known within ± 10°C. Experiments were quenched by removing the vessels from the furnace. The cooling rate was increased by blowing compressed air around the vessel with isobaric decompression, resulting in a quench rate of 250°C/min.

Electron microprobe analyses

Mineral and glass compositions were determined with an electron microprobe Cameca Camebax SX100 at the University of Hannover, Germany. Analytical conditions were 15 kV, 6 nA for glass analyses, and 10 nA for apatite and anhydrite analyses. The beam was defocused to at least 20 μm diameter for glass analysis. For crystalline phases, the beam spot was defocused by no more than 2–3 μm. All elements were analyzed during 10 s except sulfur (60 s) and fluorine (30 s) for apatite and glass and phosphorus (30 s) and calcium (30 s) for glass. Sulfur and phosphorus were analyzed using a large PET crystal. Peak search was performed for SKα radiation for sulfur analyses in glasses and was found to be close to sulfate sulfur and therefore close to the anhydrite standard, which is reasonable at oxidizing conditions (Carroll and Rutherford 1988). Standards used for calibration were albite for Na, wollastonite for Si (for mineral and glass) and Ca (for glass), apatite for Ca (for apatite), F and P (for apatite and glass), orthoclase for K, anhydrite for Ca (anhydrite) and S (anhydrite, apatite and glass). The standard deviations for apatite and glass analyses considered in this study (10–18 analysis points) incorporate both X-ray counting error and range of determined values. No sulfur was detected in Au and AuPd capsule even at the interface between glass and capsule. The water content of experimental glass is determined by difference, using standards of rhyolitic glass with different water contents (0 to 8 wt.% H_2O) following the method described in Devine et al. (1995) and Koepke (1997).

Experimental results

Run products—apatite saturation

Apatite and glass are present in all experimental products (Table 2). Anhydrite is only observed in one S-bearing experiment performed at 800 °C (both crystallization and dissolution experiments). The major differences observed between S-bearing and S-free run products were the phase morphologies and apatite abundances in both crystallization and dissolution experiments (Figs. 1 and 2). In all crystallization experiments, apatite crystallized as euhedral prismatic crystals in S-free charges, whereas it occurs mainly as isolated grains in glass or formed a cluster of 4–5 crystals in S-bearing charges (Fig. 1). The proportion of crystallized apatite is higher in S-free runs than in S-bearing runs (Table 2). In S-bearing runs, most of the apatite crystals are 5–8 μm size at 800 °C and the crystal size increases with an increase in temperature, up to 20–40 μm at 1,100 °C (Fig. 1). At 800 °C, anhydrite crystallized as isolated sub-euhedral crystal (~10 μm) close to apatite. In dissolution charges, apatite crystals are partially dissolved but still have a sharp shape (Fig. 2). Apatite crystals are less abundant in the S-bearing melt
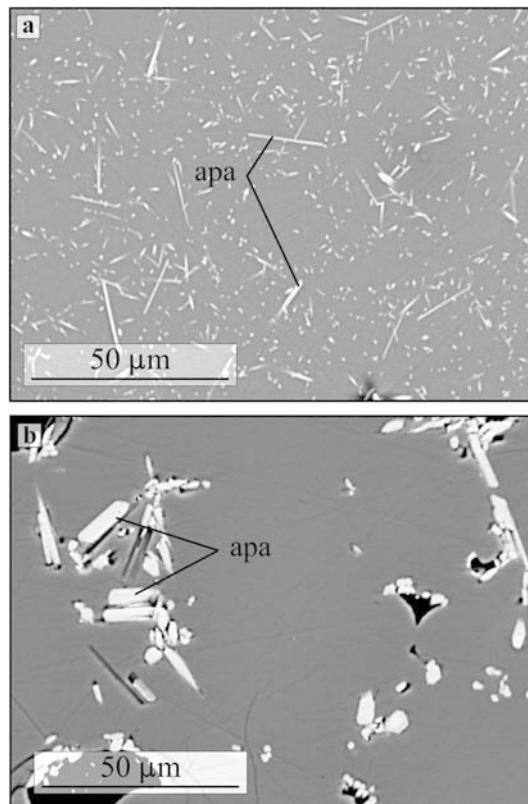

Fig. 1a,b Back-scattered electron photographs of charges from crystallization experiments. (a) #50, 1,100 °C—NNO + 3.7; (b) #51, 1,100 °C—NNO + 3.7, + 0.5 wt.% S
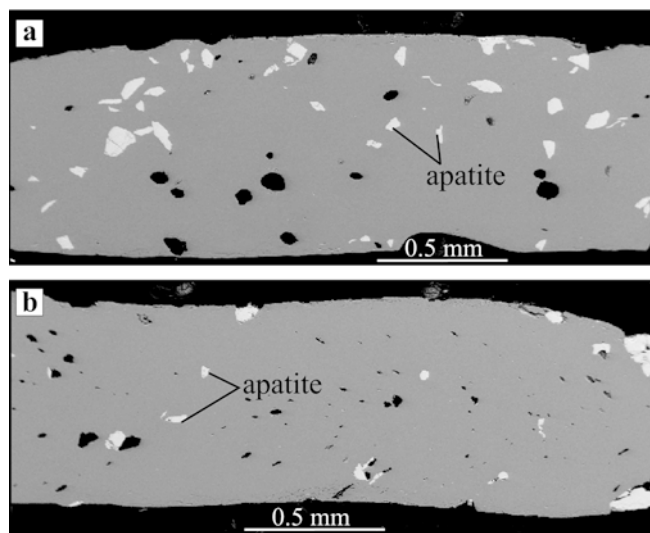
Fig. 2a,b Back-scattered electron photographs of charges from dissolution experiments. The pictures show 70% of the longitudinal sections along the capsules. (a) #52, 1,100 °C—NNO + 3.7; (b) #53, 1,100 °C—NNO + 3.7, + 0.5 wt.% S. Assuming that there is no lateral segregation of apatite, the pictures clearly show that apatite is less abundant in the S-bearing run (b)

(Fig. 2b) than in the S-free melt (Fig. 2a). As observed in crystallization runs, anhydrite crystallized as sub-euhedral crystals around apatite at 800°C. A least squares
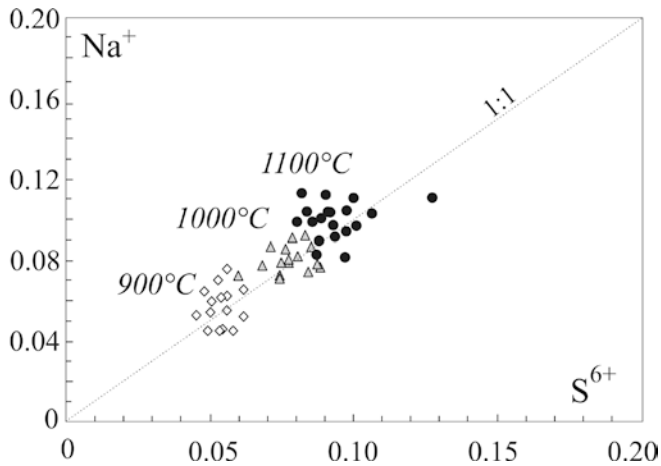
Fig. 3 S^{6+} vs. Na^+ of apatite from crystallization experiments. The 1:1 curve represents the sulfate exchange reaction in apatite ($S^{6+} + Na^+ <->P^{5+} + Ca^{2+}$; Liu and Comodi 1993)

regression mass balance calculation ($\Sigma r^2 < 0.2$) was used to estimate the proportion of crystallized and dissolved apatite (Table 2). As observed petrographically, less apatite crystallized (and more are dissolved in dissolution experiments) in S-bearing charges ($\sim 2.9 \pm 0.2$ wt.% at 1,000 °C) than in S-free charges ($\sim 3.2 \pm 0.2$ wt.% at 1,000 °C) and the proportion of crystallized apatite increases with decreasing temperature (e.g. 2.3 to 3.1 wt.% from 1,100 to 900 °C in S-bearing charges, Table 2).

Apatites from crystallization experiments are fluorapatites with composition close to the composition of starting apatite (Tables 1 and 3). In S-bearing runs, the sulfur concentration in apatite increases with an increase in temperature from 0.44 wt.% SO_3 (1,760 ppm S) at 900 °C to 0.72 wt.% SO_3 (2,880 ppm S) at 1,100 °C (Fig. 3). In large apatites, rim and core composition are identical within analytical error. Structural formula suggest that sulfur substitutes into the tetrahedral site forming SO_4^{2-} ion, and the strong positive correlation between Na^+ and S^{6+} at an atomic ratio of one (Fig. 3) suggests that the charge balance is maintained through the coupled substitution $S^{6+} + Na^+$ $P^{5+} + Ca^{2+}$ (cf. Liu and Comodi 1993). At 800 °C, profiles of phosphorus content analyzed close to apatite are not completely flat, suggesting that the equilibrium was not entirely reached. However, it can be noted that the sulfur content in apatite at 800 °C (~ 0.72 wt.% SO_3 ($\sim 2,880$ ppm S), Table 3) is higher than the sulfur content in apatite at 900 °C.

Phosphorus solubility in melt and attainment of equilibrium

The P_2O_5 content of glass is listed in Tables 4 and 5. The small standard deviations attest of the uniformity of phosphorus distribution in the glasses. In all crystallization and dissolution charges, melts have a Ca/P ratio close to apatite stoichiometry except in the run where apatite coexists with anhydrite (Ca/P$\sim$0.2, Tables 4 and 5). In dissolution experiments, flat phosphorus profiles in glass surrounding apatite crystals suggest a close approach to chemical equilibrium for all experiments except for the S-bearing dissolution experiment at 800 °C (#49, Table 2). The best evidence of equilibrium in our experiments was the identical phosphorus content in melts from crystallization and dissolution

Table 3 Analyses of apatite from crystallization experiments

Run	#47	#34	#35	#26	#27	#50	#51
T (°C)	800	900	900	1,000	1,000	1,100	1,100
	n = 4 (s.d.)	n = 1	n = 10 (s.d.)	n = 2 (s.d.)	n = 14 (s.d.)	n = 2 (s.d.)	n = 10 (s.d.)
SiO_2	0.15 (0.10)	0.71	0.53 (0.17)	0.87 (0.27)	0.34 (0.13)	1.44 (0.43)	0.48 (0.21)
CaO	54.75 (0.8)	57.70	55.48 (0.51)	57.60 (0.84)	57.62 (0.48)	54.19 (0.32)	54.16 (1.07)
Na_2O	0.18 (0.03)	0.03	0.19 (0.04)	0.02 (0.02)	0.25 (0.02)	0.11 (0.01)	0.30 (0.03)
P_2O_5	41.36 (0.74)	40.12	40.82 (0.66)	41.65 (0.74)	40.62 (0.74)	41.19 (0.39)	40.76 (0.68)
SO_3	0.72 (0.15)	–	0.44 (0.02)	—	0.64 (0.07)	—	0.72 (0.06)
S (ppm)	2,881 (607)	–	1,780 (95)	—	2,559 (282)	—	2,884 (227)
K_2O	0.10 (0.03)	0.12	0.21 (0.03)	0.20 (0.05)	0.15 (0.03)	0.24 (0.02)	0.15 (0.04)
F	3.61	3.50	3.53 (0.06)	3.51 (0.02)	3.52 (0.17)	3.47 (0.05)	3.54 (0.08)
Cl	–	–	–	–	–	–	–
Total	100.66	102.18	101.21	101.86	101.09	100.85	100.07
O-F,Cl	1.52	1.47	1.48	1.47	1.48	1.46	1.49
Total	99.14	100.71	99.73	101.22	100.47	99.39	98.58
Si	0.03	0.12	0.09	0.14	0.06	0.24	0.08
Ca	9.92	10.42	10.03	10.17	10.28	9.78	9.85
Na	0.06	0.01	0.06	0.00	0.08	0.03	0.10
P	5.92	5.73	5.83	5.81	5.72	5.87	5.86
S^{6+}	0.06	–	0.06	0.00	0.08	–	0.09
F	0.96	0.93	0.94	0.93	0.94	0.93	0.95
Cl	0.00	0.00	0.00	0.00	0.00	0.00	0.00
OHc	0.04	0.07	0.06	0.07	0.06	0.07	0.05
Total	16.98	17.28	17.06	17.12	17.22	16.93	16.98

Structural formula determined using 25(O,OH,F,Cl); OHc: calculated OH assuming F + Cl + OH = 1; n: number of analyses; s.d.: standard deviation = X-ray counting error and range of determined values

Table 4 Analyses of glasses from crystallization experiments

Run	#46	#47	#34	#35	#26	#27	#50	#51
T(°C)	800	800	900	900	1000	1000	1100	1100
	n = 8 (s.d.)	n = 8 (s.d.)	n = 8 (s.d.)	n = 8 (s.d.)	n = 10 (s.d.)	n = 18 (s.d.)	n = 10 (s.d.)	n = 9 (s.d.)
SiO_2	73.09 (0.8)	71.52 (0.38)	72.33 (0.28)	72.97 (0.15)	71.90 (0.80)	72.80 (0.29)	72.70 (0.23)	72.66 (0.37)
Al_2O_3	11.65 (0.22)	11.69 (0.07)	11.56 (0.07)	11.76 (0.04)	11.70 (0.2)	11.67 (0.13)	11.89 (0.11)	11.78 (0.09)
CaO	0.22 (0.03)	0.11 (0.01)	0.28 (0.02)	0.27 (0.02)	0.35 (0.05)	0.36 (0.04)	0.66 (0.03)	0.65 (0.03)
Na_2O	3.17 (0.2)	3.30 (0.11)	3.25 (0.20)	3.19 (0.07)	3.12 (0.19)	3.24 (0.15)	3.65 (0.07)	3.55 (0.12)
K_2O	4.03 (0.32)	4.40 (0.04)	4,48 (0.07)	4.62 (0.04)	4.38 (0.18)	4.59 (0.07)	4.45 (0.05)	4.49 (0.06)
P_2O_5	0.14 (0.02)	0.59 (0.06)	0.16 (0.02)	0.20 (0.03)	0.18 (0.02)	0.26 (0.04)	0.39 (0.04)	0.47 (0.04)
SO_3	–	0.09 (0.02)	–	0.03 (0.02)	–	0.09 (0.02)	–	0.16 (0.01)
S (ppm)	–	353 (32)	–	125 (61)	–	344 (60)	–	646 (41)
Total	92.30	91.78	92.04	93.03	91.63	93.02	93.74	93.76
H2Oc	5.14 (0.48)	5.82 (0.35)	5.70 (0.30)	4.90 (0.14)	6.92 (0.80)	4.97 (0.29)	4.22 (0.25)	4.30 (0.37)
ASI	1.12 (0.04)	1.12 (0.03)	1.12 (0.04)	1.10 (0.01)	1.17 (0.07)	1.08 (0.04)	0.98 (0.01)	0.99 (0.01)
A/CNK	1.07 (0.03)	1.1 (0.03)	0.85 (0.02)	0.84 (0.01)	1.05 (0.06)	0.83 (0.02)	0.80 (0.01)	0.80 (0.01)
Ca/P	2.04 (0.40)	0.25 (0.02)	1.47 (0.49)	1.75 (0.34)	2.43 (0.31)	1.42 (0.80)	2.17 (0.29)	1.74 (0.13)

ASI: alumina saturation index (AI/(Ca + Na + K) mol. prop.); s.d. standard deviation = X-ray counting error and range of determined values; *: equilibrium not reached; H2Oc: H_2O calculated (see text); n: number of analyses

Table 5 Analyses of glasses from dissolution experiments

Run	#48	#49*	#36	#37	#28	#29	#52	#53
T(°C)	800	800	900	900	1000	1000	1100	1100
	n = 8 (s.d.)	n = 8 (s.d.)	n = 8 (s.d.)	n = 8 (s.d.)	n = 18 (s.d.)	n = 18 (s.d.)	n = 18 (s.d.)	n = 13 (s.d.)
SiO_2	71.67 (0.47)	71.76 (0.18)	72.38 (0.14)	72.68 (0.19)	72.57 (0.52)	72.49 (0.51)	71.79 (0.81)	72.14 0.90
Al_2O_3	11.74 (0.08)	11.90 (0.04)	11.68 (0.12)	11.72 (0.09)	11.54 (0.21)	11.65 (0.13)	11.73 (0.09)	11.81 (0.09)
CaO	0.10 (0.02)	0.07 (0.01)	0.15 (0.03)	0.16 (0.02)	0.27 (0.03)	0.30 (0.05)	0.51 (0.03)	0.49 (0.05)
Na_2O	3.48 (0.11)	3.44 (0.06)	3.28 (0.08)	3.42 (0.14)	3.29 (0.10)	3.20 (0.13)	3.59 (0.11)	3.62 (0.08)
K_2O	4.53 (0.05)	4.54 (0.01)	4.55 (0.10)	4.57 (0.07)	4.56 (0.12)	4.48 (0.10)	4.54 (0.08)	4.50 (0.07)
P_2O_5	0.12 (0.02)	0.55 (0.10)	0.18 (0.02)	0.20 (0.03)	0.24 (0.03)	0.31 (0.05)	0.39 (0.03)	0.44 (0.04)
SO_3	–	0.07 (0.01)	–	0.04 (0.01)	–	0.12 (0.03)	–	0.16 (0.02)
S (ppm)	–	363 (52)	–	160 (50)	–	487 (111)	–	637 (76)
Total	91.68	92.40	92.33	92.83	92.47	92.33	92.63	93.19
H2Oc	5.39 (0.30)	5.36 (0.20)	5.42 (0.23)	5.05 (0.23)	5.31 (0.47)	5.24 (0.46)	5.19 (0.69)	4.78 (0.80)
ASI	1.09 (0.02)	1.11 (0.01)	1.10 (0.03)	1.08 (0.03)	1.07 (0.03)	1.09 (0.02)	1.00 (0.02)	1.01 (0.02)
A/CNK	1.07 (0.02)	1.10 (0.01)	1.06 (0.03)	1.05 (0.02)	1.02 (0.03)	1.10 (0.03)	0.93 (0.02)	0.94 (0.02)
Ca/P	1.10 (0.25)	0.18 (0.05)	1.21 (0.25)	1.14 (0.30)	1.41 (0.28)	1.28 (0.30)	1.65 (0.13)	1.59 (0.26)

ASI: alumina saturation index (Al/(Ca + Na + K) mol. prop.); s.d. standard deviation = X-ray counting error and range of determined values; *: equilibrium not reached; H2Oc: H_2O calculated (see text); n: number of analyses

experiments. The phosphorus content in S-free runs at 1,100 °C (#52, $P_2O_5 = 0.39$ wt.%) is close to that determined at 1,100 °C for metaluminous compositions by Harrison and Watson (1984) ($P_2O_5 = 0.35$ wt.%). At this temperature, the bulk melt composition of run #52 is similar to the composition (especially the CaO content, see discussion) used by Harrison and Watson (1984) to calibrate the geothermometer.

In both crystallization and dissolution experiments, the solubility of phosphorus is slightly higher in S-bearing melts than in S-free melts (Figs. 4 and 5). In crystallization experiments at 1,000 °C, the P_2O_5 content in the glass ranges from 0.22 to 0.30 wt.% in the S-bearing run and 0.16 to 0.22 wt.% in the S-free run (Fig. 4). Similarly, in dissolution runs at 1,000 °C, the P_2O_5 content is higher in the S-bearing melt (0.28–0.38 wt.%) than in the S-free melt (0.21–0.30 wt.%). Phosphorus solubility increases with temperature, in agreement with previous experimental studies (e.g. Harrison and Watson 1984; Pichavant et al. 1992).

To determine cation affinities in haplogranitic melt, one apatite dissolution experiment has been performed at 1,000 °C for 24 h. The equilibrium was not reached and the melt is not homogeneous. The back-scattered electron images show no anhydrite crystals in the melt. Analyses of sulfur, calcium and phosphorus of the melt are shown in Harker diagrams (Fig. 6) rather than profiles that represent complex dissolution intermingling far from apatites. There is a clear positive correlation between SO_3 and CaO. Since the starting glass contained sulfur and was devoid of CaO, this positive correlation cannot be related to identical (coupled) diffusivity of Ca and S but rather indicates the possible formation of Ca-S-bearing complexes in the melt.
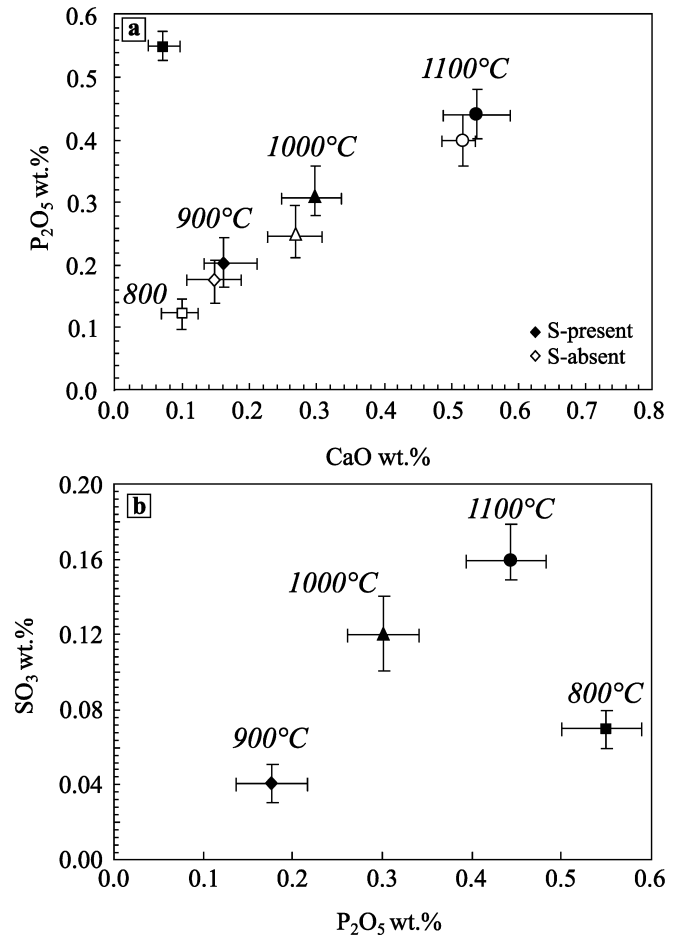
Sulfur solubility in melts

Sulfur is distributed between apatite, ± anhydrite, melt and fluid. The sulfur content in the fluid phase has been
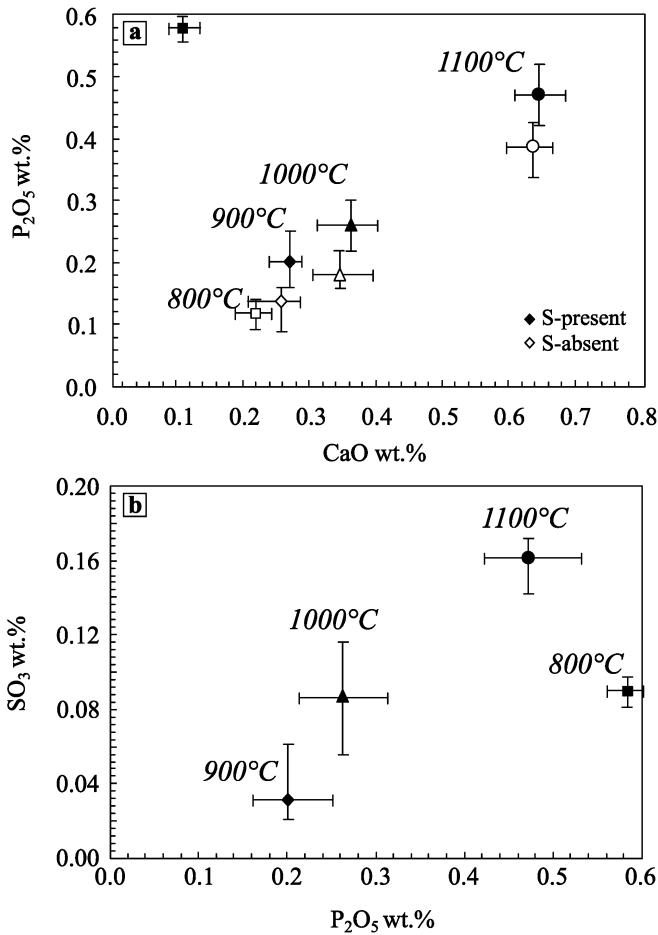
Fig. 4a,b (a) CaO vs. P_2O_5 and (b) P_2O_5 vs. SO_3 content in the melt from apatite crystallization experiments. The *symbols* are the average values of 10–18 analysis points. The *error bars* integrate both X-ray counting error and range of determined values

Fig. 5a,b (a) CaO vs. P_2O_5 and (b) P_2O_5 vs. SO_3 content in the melt from apatite dissolution experiments. Symbols and error bars: see Fig. 4

estimated by mass balance (Table 2). The sulfur content in the melt is shown versus phosphorus content in Figs. 4 and 5 (see details in Tables 4 and 5). The sulfur contents in the melts from crystallization and dissolution experiments are identical within analytical error. The sulfur solubility measured in anhydrite-undersaturated haplogranitic melts increases with increasing temperature from 0.03 wt.% SO_3 (125 ppm S) at 900 °C to 0.16 wt.% SO_3 (646 ppm S) at 1,100 °C, in agreement with previous experimental studies (Carroll and Rutherford 1987; Luhr 1990; Baker and Rutherford 1996a). The sulfur content in the fluid phase also increases as temperature decreases (7 wt.% at 1,100 °C, to 9 wt.% at 800 °C, see Table 2). These estimations allow determination of the sulfur partition coefficient between fluid and melt ($Kd_S^{fluid/melt}$). Under anhydrite-undersaturated conditions, $Kd_S^{fluid/melt}$ increases with decreasing temperature from ~100 at 1,100 °C to ~600 at 900 °C (Table 2).

At 800 °C, sulfur is distributed between apatite, silicate melt, and fluid but also anhydrite. The distribution of sulfur between the coexisting phases is therefore not directly comparable to the result obtained at 900–

1,100 °C. In addition, the crystallization of anhydrite leads to a decrease of CaO content of the melt (0.11 wt.% CaO, Table 4), which may influence the sulfur solubility. At 800 °C, the sulfur content of the melt ranges from 0.06 to 0.12 wt.% SO_3 (240 to 460 ppm S, Tables 4 and 5) which is higher than that extrapolated from high temperature anhydrite-undersaturated runs (at 900 °C, S = 125 ppm). However, the results of the 800 °C experiment need to be interpreted with caution since equilibrium distribution of phosphorus was not completely reached.

Partitioning of sulfur between apatite and melt

Although equilibrium between apatite and melt is observed for phosphorus distribution in all experiments performed at 900–1,100 °C (see above), only crystallization experiments can be used to determine sulfur distribution between apatite and melt. In dissolution experiments, the sulfur content of the residual apatite was identical to the starting apatite (nearly S-free apatite). The lines of evidence for sulfur equilibrium distribution between apatite and melt from crystallization
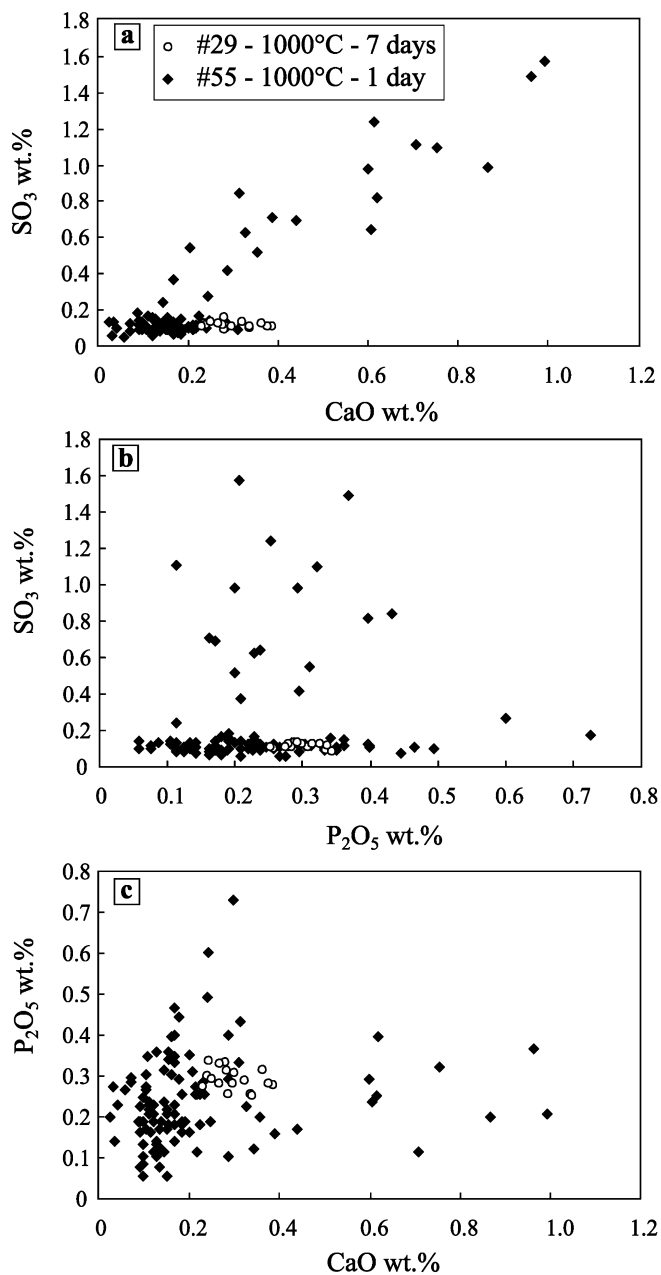
Fig. 6a–c (a) CaO vs. SO$_3$, (b) P$_2$O$_5$ vs. SO$_3$, and (c) CaO vs. P$_2$O$_5$ content in the melt from apatite dissolution experiments performed at 1,000 °C and 200 MPa. Note the scatter of the data for the one-day experiment related to non-equilibrium conditions. Note also the good correlation between CaO and SO$_3$ for the one-day experiment

experiments are: no compositional zonation is observed in large apatite; the apatites are stoichiometric and their compositions agree with the exchange reaction: S^{6+} + Na^+ P^{5+} + Ca^{2+} (Fig. 3). In crystallization anhydrite-undersaturated experiments, sulfur content in both melt and apatite increases with temperature (Fig. 7). The partition coefficient of sulfur between apatite and melt (Kd$_S$$^{apatite/melt}$) increases with a decrease in temperature from 4.5 at 1,100 °C to 7.4 at 1,000 °C and 14.2 at 900 °C (Fig. 8). The crystallization of anhydrite at

800 °C hinders the determination of the partition coefficient of sulfur between apatite and melt at low temperature for an anhydrite-undersaturated melt. However, despite that equilibrium was not reached at 800 °C, the partition coefficient of sulfur between apatite and anhydrite-saturated melt can be estimated at 8 and is very close to those determined by Baker and Rutherford (1996b) at 760 °C on anhydrite-saturated dacite and trachyandesite of Pinatubo and El Chichòn (Fig. 8). It can be noted that Peng et al. (1997) determined a higher sulfur partition coefficient of 33 on El Chichòn trachyandesite at 800 °C. This discrepancy is discussed below.

Discussion

Apatite crystallization

Crystallization mechanisms result from an intricate interplay of kinetics, time, and temperature (Marsh 1998). In S-free and S-bearing crystallization runs, time and temperature are identical and the difference in apatite nucleation and size must result from kinetic effects. The rate of nucleation depends most strongly on the diffusivity of species in the melt and the nucleation process. As the addition of a small amount of sulfur (0.5 wt.% S) does not dramatically change the viscosity of the melt, it is not expected to affect the diffusion of phosphorus in the melt. The difference in apatite size and nucleation between S-bearing and S-free runs may be then related to change in nucleation process or kinetics.

Sulfur solubility and distribution between apatite and melt

Sulfur solubility in melts depends mainly on temperature, pressure, oxygen fugacity, water content, and melt composition (e.g. Fe, Si) (e.g. Carroll and Webster 1994). Our experiments have been performed at water-saturated and oxidizing conditions and the charges performed at T≥900 °C are anhydrite-undersaturated, whereas anhydrite crystallized at 800 °C. The sulfur content in the melt increases with increasing temperature from 900 to 1,100 °C, in agreement with previous experimental data. However these sulfur contents (0.03–0.16 wt.% SO$_3$) correspond to lower values than those previously determined for hydrous anhydrite-saturated rocks at oxidizing conditions (Carroll and Rutherford 1987; Luhr 1990; Baker and Rutherford 1996a) because sulfur saturation is not reached in anhydrite-free runs. On the other hand, similar values to those previously determined by experiments (Carroll and Rutherford 1987; Luhr 1990; Baker and Rutherford 1996a) have been obtained for the anhydrite-saturated run performed at 800 °C. This suggests that at this condition, i.e. sulfur-saturated, oxidizing condition, and low temperature (800 °C), there is little difference in sulfur sol-

Fig. 7 Sulfur content in the melt vs. sulfur content in apatite from crystallization experiments (this study: *black symbols*). The point at 800 °C (*black circle*) seems anomalous relative to the 900–1,100 °C trend but this experiment is anhydrite-saturated, whereas anhydrite is not present in the other experiments. Note also that the data of Peng et al. (1997) at 800 °C does not fit with the general trend (for explanation see text). *Symbols and error bars*: see Fig. 4
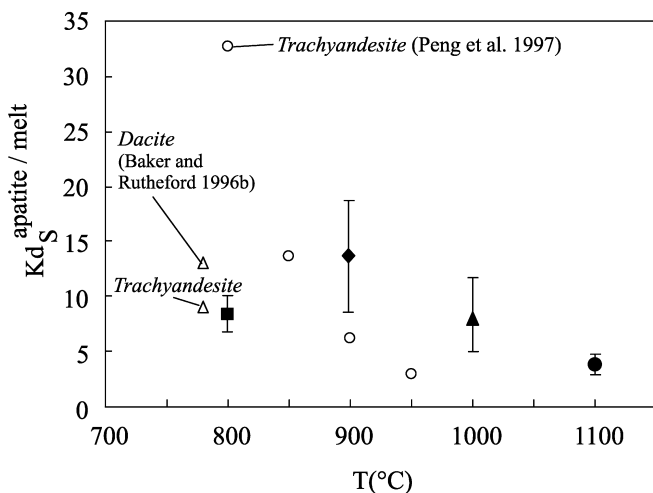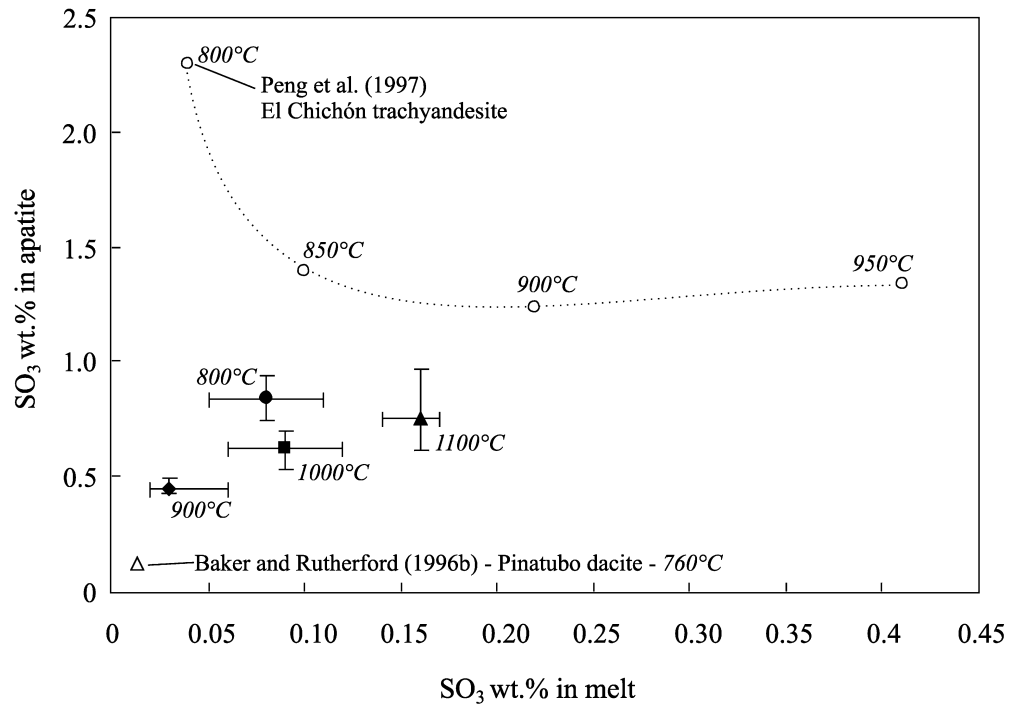
Fig. 8 Sulfur partition coefficient between apatite and melt as a function of temperature (this study: *black symbols*). *Symbols and error bars*: see Fig. 4

ubility between our haplogranitic composition and trachyandesitic or rhyolitic natural rocks, despite a range of almost 6 wt.% in FeO variation among the samples. As proposed by Ducea et al. (1999), the bulk iron content has little effect on sulfur solubility under these conditions.

Experimental data from Baker and Rutherford (1996b) on El Chichòn trachyandesite and Pinatubo dacite suggest a sulfur partition coefficient between apatite and melt of 9 and 13, respectively, at 760 °C. These values are close to our sulfur partition coefficient determined in the anhydrite-saturated run at 800 °C ($Kd_S^{apatite/melt} \sim 8$), suggesting a small effect of melt composition on the sulfur partition coefficient. In con-

trast, Peng et al. (1997) reported a higher sulfur partition coefficient of about 33 for experiments at 800 °C on the El Chichòn trachyandesite. Peng et al. (1997) have also determined the distribution of sulfur between apatite and melt at higher temperature. $Kd_S^{apatite/melt}$ increases from 3 to 33 with decreasing temperature from 950 to 800 °C (Fig. 8). All experiments mentioned above are anhydrite-saturated. The marked difference between the sulfur partition coefficient determined by Baker and Rutherford (1996b) and those of Peng et al. (1997) on the same compositions (El Chichòn) at similar P-T conditions can only be explained by experimental problems during apatite crystallization. Experimental products used by Peng et al. (1997) at 800 °C were first annealed at 1,100 °C and temperature was then decreased (Luhr 1990). During this temperature decrease, apatite may have started to crystallize which may explain the sulfur zonation observed in the apatites (Peng et al. 1997). Thus, the core composition of apatite may not reflect the equilibrium sulfur content at low temperature. Further indications suggesting experimental problems at low temperature is shown in Fig. 7. The correlation between S in apatite and S in melt obtained from Peng et al. (1997) and Luhr (1990) shows a strong increase of S in apatite with decreasing S in melt. This is unrealistic because such a relationship should pass through the origin. On the other hand, our anhydrite-saturated data at 800 °C, data of Baker and Rutherford (1996b) at 760 °C, and the high temperature data of Peng et al. (1997) (900–950 °C) show a consistent trend with concomitant decrease of S in apatite and S in melt (Fig. 7).

Figure 8 shows a synthesis of the available sulfur partition coefficients between apatite and melt. Our $Kd_S^{apatite/melt}$ at T≥900 °C are slightly higher than those

determined by Peng et al. (1997) which may be due to anhydrite-undersaturated conditions in our experiments. In addition, the melt composition of the dataset of Peng et al. (1997) is not identical for all temperatures (e.g. $SiO_2 = 70$ to 61 wt.% from 800 to 950 °C; Luhr, 1990). The increase of $Kd_S^{apatite/melt}$ with temperature is however consistent with the trend observed by Peng et al. (1997). The difference in $Kd_S^{apatite/melt}$ observed between anhydrite-saturated and anhydrite-undersaturated melts suggests that the $Kd_S^{apatite/melt}$ depends on the sulfur content in the melt and not significantly on the bulk composition (approximately same $Kd_S^{apatite/melt}$ for Pinatubo dacite and haplogranite).

Phosphorus solubility

Previous studies have shown that phosphorus speciation in silicate melts is highly dependent on melt composition, thus implying a complex solution behavior. Spectroscopic studies of phosphatic glasses using both Raman (Gan and Hess 1992; Mysen 1992) and NMR spectroscopy (Gan and Hess 1992) have shown that P does not substitute for silica in the network, but rather it removes network modifiers to form discrete phosphate complexes, thus polymerizing the remaining portion of the silica network. Furthermore, the high rare earth element (REE) content of natural apatites, the enrichment of REEs in P_2O_5-rich immiscible liquids (Ryerson and Hess 1978), and studies of the effects of P addition on an aluminum-bearing system (Gan and Hess 1992; Mysen 1992; Gwinn and Hess 1993; London et al. 1993) all suggest a strong complexing of P and M^{3+} cations.

Harrison and Watson (1984) proposed a geothermometer based on an apatite solubility model. Pichavant et al. (1992) improved this model by incorporating the role of non-charge balanced Al^{3+} cations (excess aluminum). However, our investigated composition has a very low excess aluminum (ASI = 1.03) and the phosphorus concentration can be used only to test the apatite solubility model following Harrison and Watson (1984). Results at 1,100 °C match the predicted temperature, whereas the phosphorus concentrations in the experimental melt at lower temperature are higher than predicted by the Harrison and Watson model (1984) (Fig. 9). The model underestimates the P_2O_5 content in the low temperature range. One possible explanation is that calcium concentrations (and not only Al^{3+}) in the melt influences phosphorus solubility. The investigated composition contains initially no CaO and the final CaO content is below 0.36 wt.% at T ≤ 1,000 °C. In contrast the initial rhyolitic compositions used in the model of Harrison and Watson (1984) contain 0.52 to 1.57 wt.% CaO (Green and Watson 1982). The final CaO content of our experiment at 1,100 °C is 0.65 wt.%. This may explain the good agreement between experimental and predicted temperature at 1,100 °C. Thus, our results suggest that P solubility is higher at low Ca activity, which is in agreement with observations of Bea et al.
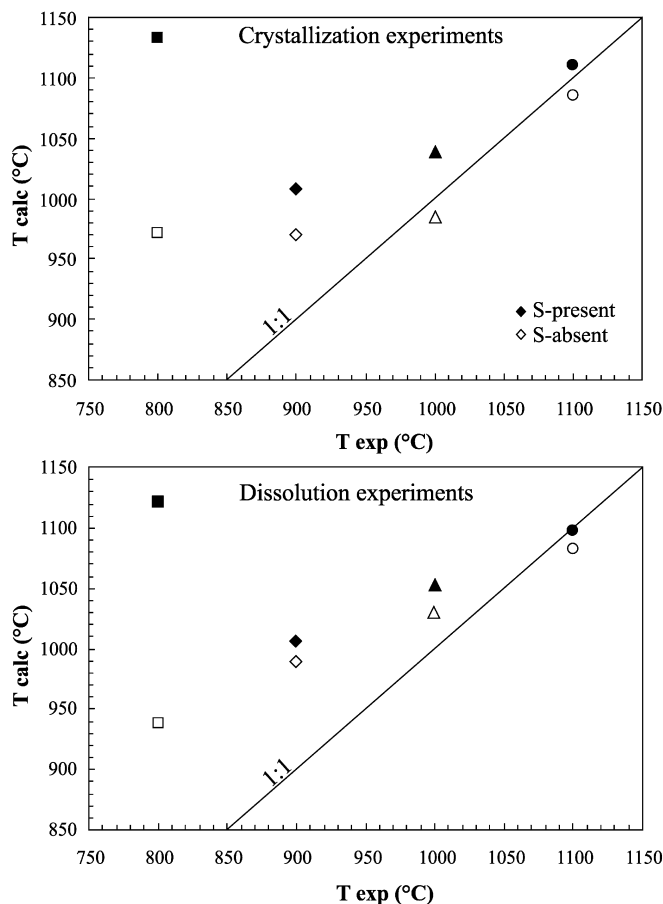
Fig. 9 Comparison between experimental temperature (*T exp*) and calculated temperature (*T calc*) using the model of Harrison and Watson (1984) based on the P_2O_5 content of the melt

(1992) and with data in Ca-free systems showing that up to 5.1 wt.% P_2O_5 can be dissolved in haplogranitic melt at 850 °C (Holtz et al. 1993).

It can be noted that the phosphorus content in our apatite-saturated experiments is always higher in S-bearing charges. This results in higher saturation temperatures when using the model of Harrison and Watson (1984) (Fig. 9). The two sulfur bearing-experiments at 800 °C depart strongly from the model but in this case the charges were anhydrite-saturated. This indicates that the presence of sulfur may influence the apatite solubility geothermometers, at least in Ca-poor melts, leading to an overestimation of the temperature. An explanation would be the formation of Ca-SO_4 complexes (anhydrite like complex) that would decrease the activity of Ca and increase the solubility of apatite. If this is true, it means that S should also increase solubility of other Ca-bearing minerals such as An-rich plagioclase.

Conclusion on sulfur distribution between apatite and melt

The results of this study show that, under oxidizing conditions, sulfur content in apatite can be used to track

the sulfur content in coexisting melt and record sulfur evolution during magmatic process. The dominant parameters controlling the sulfur partition coefficient are (1) the temperature and (2) the bulk sulfur content. Up to now, there is no information on the possible effect of changing oxygen fugacity. (1) The sulfur partition coefficient between apatite and haplogranitic melt increases with increasing temperature in agreement with previous results (Peng et al. 1997). (2) In this study we show that S in apatite increases with increasing sulfur content in the melt. This contrasts with previous observations of Peng et al. (1997) and the discrepancy may be due to a kinetic problem in previous experiments.

The effect of the bulk melt composition (rhyolite to andesite) on the distribution of sulfur between apatite and melt is difficult to assess from the available experimental data. However, there is no evidence for a strong compositional dependence on the sulfur partition coefficient when comparing data obtained with rhyolitic melt (this study) and trachyandesitic and dacitic melts (Baker and Rutherford 1996b). A possible cation which may influence the sulfur partitioning is Ca, considering that sulfur solubility in silicate melts is influenced by the calcium content in the melt (Ducea et al. 1999), and that there is evidence for the formation of Ca-S complexing cations. It is emphasized that these observations are only valid at oxidizing conditions where sulfur occurs as sulfate in the melt.

References

Bagdassarov NS, Dingwell DB (1993) Frequency dependent rheology of vesicular rhyolite. J Geophys Res, B, Solid Earth and Planets 98(4):6477–6487

Baker L, Rutherford MJ (1996a) Sulfur diffusion in rhyolite melts. Contrib Mineral Petr 123:335–344

Baker L, Rutherford MJ (1996b) Crystallization of anhydrite-bearing magmas. In: M Brown et al. (eds), Origin of granites and related rocks. Geological Society of America Special Paper, pp 243–250

Bea F, Fershtater G, Corretgé LG (1992) The geochemistry of phosphorus in granite rocks and the effect of aluminium. Lithos 29(1–2):43–56

Berndt J, Holtz F, Koepke J (2001) Experimental constraints on storage conditions in the chemically zoned phonolitic magma chamber of the Laacher See volcano. Contrib Mineral Petr 140(4):469–486

Berndt J, Koepke J, Holtz F (2004) Influence of H₂O and oxygen fugacity on differentiation of MORB at 200 MPa. J Petrology (in press)

Blank JG, Brooker RA (1994) Experimental studies of carbon-dioxide in silicate melts-solubility, speciation, and stable carbon-isotope behavior. In: Carroll MR, Holloway JR (eds), Volatiles in magmas. Reviews in Mineralogy, Mineralogical Society of America, Washington, DC, pp 157–186

Carroll MR, Rutherford MJ (1987) The stability of igneous anhydrite: experimental results and implications for sulfur behavior in the 1982 El Chichòn trachyandesite and other evolved magmas. J Petrology 28:781–801

Carroll MR, Rutherford MJ (1988) Sulfur speciation in hydrous experimental glasses of varying oxidation states: results from measured wavelength shifts of sulfur X-rays. Am Mineralogist 73:845–849

Carroll MR, Webster JD (1994) Solubilities of sulfur, noble gases, nitrogen, chlorine, and fluorine in magmas. In: Carroll Michael R, Holloway John R (eds), Volatiles in magmas. Reviews in Mineralogy, Mineralogical Society of America, Washington, DC, pp 231–279

Devine JD, Gardener JE, Brack HP, Layne GD, Rutherford MJ (1995) Comparison of microanalytical methods for estimating H₂O contents of silicic volcanic glasses. Am Mineralogist 80:319–328

Ducea MN, McInnes BIA, Wyllie PJ (1999) Experimental determination of composition dependence of hydrous silicate melts on sulfate solubility. Eur J Mineral 11(1):33–43

Gan H, Hess PC (1992) Phosphate speciation in potassium aluminosilicate glasses. Am Mineralogist 77(5–6):495–506

Green TH, Watson EB (1982) Crystallization of apatite in natural magmas under high-pressure hydrous conditions, with particular reference to orogenic rock series. Contributions to Mineralogy and Petrology 79(1):96–105

Gwinn R, Hess PC (1993) The role of phosphorus in rhyolitic liquids as determined from the homogeneous iron redox equilibrium. Contrib Mineral Petr 113(3):424–435

Harrison TM, Watson EB (1984) The behavior of apatite during crustal anatexis; equilibrium and kinetic considerations. Geochimica et Cosmochimica Acta 48(7):1,467–1,477

Holtz F, Dingwell DB, Behrens H (1993) Effects of F, B₂O₃ and P₂O₅ on the solubility of water in haplogranite melts compared to natural silicate melts. Contrib Mineral Petr 113(4):492–501

Holtz F, Johannes W, Tamic N, Behrens H (2001) Maximum and minimum water contents of granitic melts generated in the crust: a reevaluation and implications. Lithos 56(1):1–14

Johnson MC, Anderson AT, Rutherford MJ (1994) Pre-eruptive volatile contents of magmas. In: Carroll MR, Holloway JR (eds), Volatiles in magmas. Reviews in Mineralogy, Mineralogical Society of America, Washington, DC, pp 281–330

Koepke J (1997) Analyse von wasserhaltigen silikatischen Gläsern mit der Mikrosonde: Wassergehalte und Alkaliverluste. Beih J Mineral 9:200

Liu Y, Comodi P (1993) Some aspects of the crystal-chemistry of apatites. Mineralogical Magazine 57:709–719

London D, Morgan GB, Babb HA, Loomis JL (1993) Behavior and effects of phosphorus in the system Na₂O-K₂O-Al₂O₃-SiO₂-P₂O₅-H₂O at 200 MPa (H₂O). Contrib Mineral Petr 113(4):450–465

Luhr JF (1990) Experimentally phase relations of water- and sulfur-saturated arc magmas and the 1982 eruption of El Chichòn volcano. J Petrology 31:1071–1114

Luhr JF, Carmichael ISE, Varekamp JC (1984) The 1982 eruptions of El Chichòn volcano, Chipas, Mexico: mineralogy and petrology of the anhydrite-bearing pumice. J Volcanol Geoth Res 23:69–108

Marsh BD (1998) On the interpretation of crystal size distributions in magmatic systems. J Petrology 39(4):553–599

Mysen BO (1992) Iron and phosphorus in calcium silicate quenched melts. Chem Geol 98(3–4):175–202

Papale P (1999) Modeling of the solubility of a two-component H₂O + CO₂ fluid in silicate liquids. Am Mineralogist 84(4):477–492

Parat F, Dungan MA, Streck MJ (2002) Anhydrite, pyrrhotite and sulfur-rich apatite: tracing the sulfur evolution of an Oligocene andesite (Eagle Mountain, Colorado, U.S.A.). Lithos 64:63–75

Peng G, Luhr JF, McGee JJ (1997) Factors controlling sulfur concentrations in volcanic apatite. Am Mineralogist 82:1210–1224

Pichavant M, Montel J-M, Richard LR (1992) Apatite solubility in peraluminous liquids; experimental data and an extension of the Harrison-Watson model. Geochimica et Cosmochimica Acta 56(10):3588–3861

Ryerson FJ, Hess PC (1978) Implications of liquid-liquid distribution coefficients to mineral-liquid partitioning. Geochimica et Cosmochimica Acta 42(6A):921–932

Ryerson FJ, Hess PC (1980) The role of P_2O_5 in silicate melts. Geochimica et Cosmochimica Acta 44(4):611–624

Scaillet B, Evans BW (1999) The 15 June 1991 eruption of Mount Pinatubo; I, Phase equilibria and pre-eruption P-T-fO_2 -fH_2O conditions of the dacite magmas. J Petrology 40(3):381–411

Scaillet B, Clemente B, Evans BW, Pichavant M (1998) Redox control of sulfur degassing in silicic magmas. J Geophys Res, B, Solid Earth and Planets 103(10):23,937–23,949

Stevenson RJ, Dingwell DB, Webb SL, Bagdassarov NS (1995) The equivalence of enthalpy and shear stress relaxation in rhyolitic obsidians and quantification of the liquid-glass transition in volcanic processes. J Volcanol Geoth Res 68(4):297–306

Streck MJ, Dilles JH (1998) Sulfur evolution of oxidized arc magmas as recorded in apatite from a porphyry copper batholith. Geology 26(6):523–526

Tamic N, Behrens H, Holtz F (2001) The solubility of H_2O and CO_2 in rhyolitic melts in equilibrium with a mixed CO_2-H_2O fluid phase. Chem Geol 174(1–3):333–347

Taylor JR, Wall VJ, Pownceby MI (1992) The calibration and application of accurate redox sensors. Am Mineralogist 77(3–4):284–295

Watson EB (1979) Apatite saturation in basic to intermediate magmas. Geophys Res Letters 6(12):937–940

Wolf MB, London D (1994) Apatite dissolution into peraluminous haplogranitic melts; an experimental study of solubilities and mechanisms. Geochimica et Cosmochimica Acta 58(19):4127–4145